# INVESTIGATION OF FORCED SHOCK-INDUCED SEPARATION IN A TRANSONIC CHANNEL

*N. Goffart*[1,*] - *B. Tartinville*[1] - *C. Hirsch*[1] - *S. Pirozzoli*[2]

[1] Cadence Design Systems Belgium, Chaussée de la Hulpe 189, Brussels B-1170 Belgium
[*] ngoffart@cadence.com
[2] Department of Mechanical and Aerospace Engineering, Sapienza University of Rome, via Eudossiana 18, 00184 Rome, Italy

## ABSTRACT

**This paper presents the results of an implicit large-eddy simulation of the transonic flow over a bump. The conditions are chosen such that the configuration reproduces actual turbomachinery flows: a shock wave develops as in a transonic passage and a fluctuating backpressure is imposed to mimic the perturbations coming from a downstream row. The aim of the study is to investigate the influence of the forced conditions on the flow field, with an emphasis on the harmonic component of the turbulent stresses in the recirculation region. Results indicate that all the flow features (shock motion, wall static pressure, separation and reattachment points) respond primarily to the forcing frequency. Phase-averaging is employed to extract the coherent component of the flow. It is shown that the harmonic turbulent stresses are organized into different structures and are non-negligible with respect to the mean component.**

## KEYWORDS

channel flow, transonic, forced oscillation, turbulence

## NOMENCLATURE

| | |
|---|---|
| $B_l$ | bump length [m] |
| $\delta_0$ | reference boundary layer thickness [m] |
| $\Delta_x, \Delta_y, \Delta_z$ | grid resolution in the streamwise, wall-normal and spanwise direction [m] |
| $\nu$ | kinematic viscosity [m$^2$/s] |
| $U_\infty$ | freestream velocity [m/s] |

*Abbreviations*

| | |
|---|---|
| CFL | Courant–Friedrichs–Lewy |
| DNS | Direct Numerical Simulation |
| FFT | Fast Fourier Transform |
| (I)LES | (Implicit) Large-Eddy Simulation |
| PDF | Probability Density Function |
| (U)RANS | (Unsteady) Reynolds-Averaged Navier-Stokes |
| WPSD | Weighted Power Spectral Density |

*Superscripts*

| | |
|---|---|
| $+$ | wall unit |
| $-$ | mean component |
| $\sim$ | coherent (harmonic) component |
| $'$ | incoherent component |

 

## INTRODUCTION

As soon as transonic regime is reached in a turbomachine, a shock-wave develops on the blade suction side and interacts with the boundary layer. For a strong shock, separation of the boundary layer occurs, and the massive recirculation, amplified by the blade curvature, can drastically impact the engine efficiency. The periodic passage of a downstream row induces an oscillation of the backpressure that further affects the interaction and the turbulence in the separated region. Accounting for this unsteady potential effect at the design stage would allow an improvement in engine efficiency.

High-fidelity computational methods such as LES and DNS are suitable to predict the complex flow phenomena occurring in turbomachinery compared to (U)RANS approaches (Tucker, 2011). However, even with the increasing computational power, the cost remains high, especially if one wants to simulate the whole span of the blade. For fundamental flow physics investigation, simpler geometries such as bumps can be used.

Among the various geometries that can be found in the literature, Bron (2003) designed a new bump to study basic flow interactions in turbomachinery, both experimentally and numerically. The operating points investigated give rise to a shock-wave that interacts with the boundary layer and the influence of an oscillating backpressure on the shock motion is assessed. The frequency $f$ of the perturbation is relatively high and can reach up to 500Hz, giving a reduced frequency $f_r = fB_l/U_\infty \approx 0.4$. This order of magnitude is also encountered in turbomachinery flows (He & Ning, 1998) and means that convection and periodic fluctuations are two equally-dominant mechanisms.

Whereas the numerical investigations of Bron (2003) are performed using (U)RANS, other authors employed high-fidelity methods. With fixed backpressure in time, Wollblad et al. (2006) used LES with subgrid scale model in conditions similar to the experiment. The Reynolds number had however to be decreased by a factor of 11.25 to make the computation feasible, giving $Re = B_l U_\infty/\nu \approx 3.1 \times 10^5$. The effects of the flow conditions and the computational setup have been further examined in Wollblad et al. (2010). More recently, Brouwer (2016) performed a DNS but at a higher Mach number (0.79 against 0.7 in Bron (2003)) and at an even lower Reynolds number ($Re \approx 1.7 \times 10^5$). The impact of oscillating backpressure on the shock motion has been investigated only by Bodin and Fuchs (2008) using ILES. The results highlighted a hysteretic behavior of the shock. However, the reduced frequencies considered were one or two order(s) of magnitude lower than what could be expected in turbomachinery. The flow is thus quasi-steady and convection is the dominant mechanism.

In light of this, this paper presents the results of an ILES of the transonic flow over this bump, with backpressure fluctuating at a realistic reduced frequency. The high-order solver and the computational setup are presented in the first section. The results are examined in the second section. The influence of the oscillating backpressure is assessed with a particular emphasis on the harmonic component of turbulent stresses.

## COMPUTATIONAL METHODOLOGY

### Numerical schemes

An in-house high-order solver is employed to perform the high-fidelity simulation. The spatial discretization is based on the flux reconstruction approach introduced by Huynh (2007). The temporal derivative is computed using an explicit 5-stages fourth-order accurate Runge-Kutta scheme (Carpenter & Kennedy, 1994).

To deal with shock-wave/boundary layer interactions, an efficient shock-capturing technique

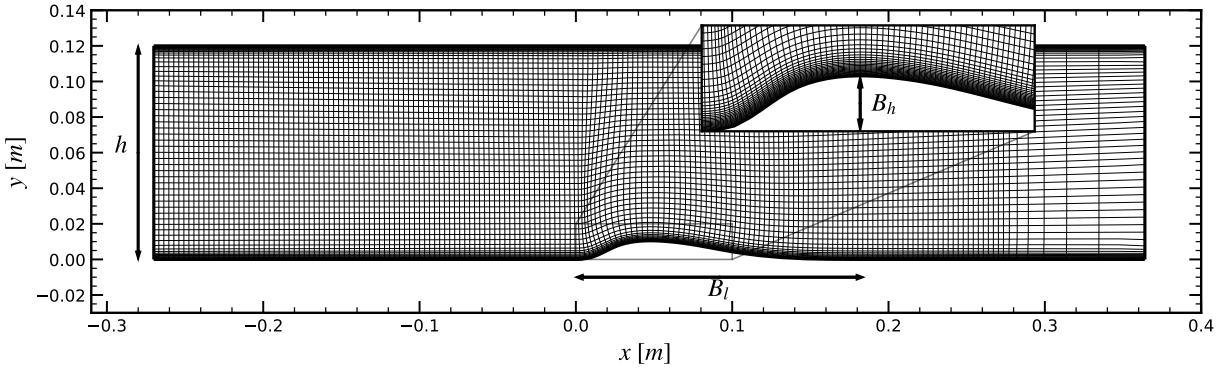


Figure 1: **Computational domain and mesh. One gridline out of two is represented in the full domain view.**

has to be used. In this work, the Laplacian artificial viscosity method of Persson and Peraire (2006) is combined with the Ducros sensor (Ducros et al., 1999). This additional step is required to discriminate the shock from the boundary layer. Indeed, artificial viscosity can damp the turbulent fluctuations in the boundary layer and has therefore to be focused around shocks only. Besides shock-capturing, the robustness is further enhanced by the use of a positivity-preserving limiter (Wang et al., 2012).

Another key feature of the solver is the prescription of turbulent inflow conditions. It is done using the digital filtering approach introduced by Klein et al. (2003) but with a 2D filter correlated in time (Adler et al., 2018; Xie & Castro, 2008). The perturbations are scaled following Lund et al. (1998).

The solver has been validated in a previous work on a canonical oblique shock-wave/boundary layer interaction (Goffart et al., 2022). It contains also more details about the shock-capturing technique and its performance.

**Flow conditions and simulation setup**

The case under investigation is the transonic flow over a bump, the geometry of which is taken from the experiment of Bron (2003). The bump length $B_l$ is 0.184m and its thickness $B_h$ is 10.48mm, whereas the wind tunnel height $h$ is 0.12m (see figure 1). The upstream conditions are a total pressure of 160kPa, a total temperature of 300K and a Mach number of 0.7. Whereas various levels of backpressure have been studied in the experiment, the focus is here for the case with a mean static pressure of 106kPa. Moreover, the backpressure is set to fluctuate in time following a sine wave of amplitude equal to 2% of the mean static pressure and of frequency equal to 500Hz. The Reynolds number based on the bump length amounts to $\approx 1.9 \times 10^5$, which is 20 times lower in comparison to the experiment. The fluid is therefore air assumed as a perfect gas but with a dynamic viscosity multiplied by the same factor.

The computational domain, depicted in figure 1, is a simple box with the bump geometry as bottom boundary. It extends from $30\delta_0$ upstream of the bump to $20\delta_0$ downstream. In the spanwise direction, the domain is $4\delta_0$ wide. Following the experimental measurements of Sigfrids (2003), the reference boundary layer thickness $\delta_0$ here is 8.95mm, measured at $x = -0.1$m. This value has also been considered in other numerical studies (Wollblad et al., 2006).

The mesh consists of hexahedra only and is also illustrated in figure 1. Using the high-

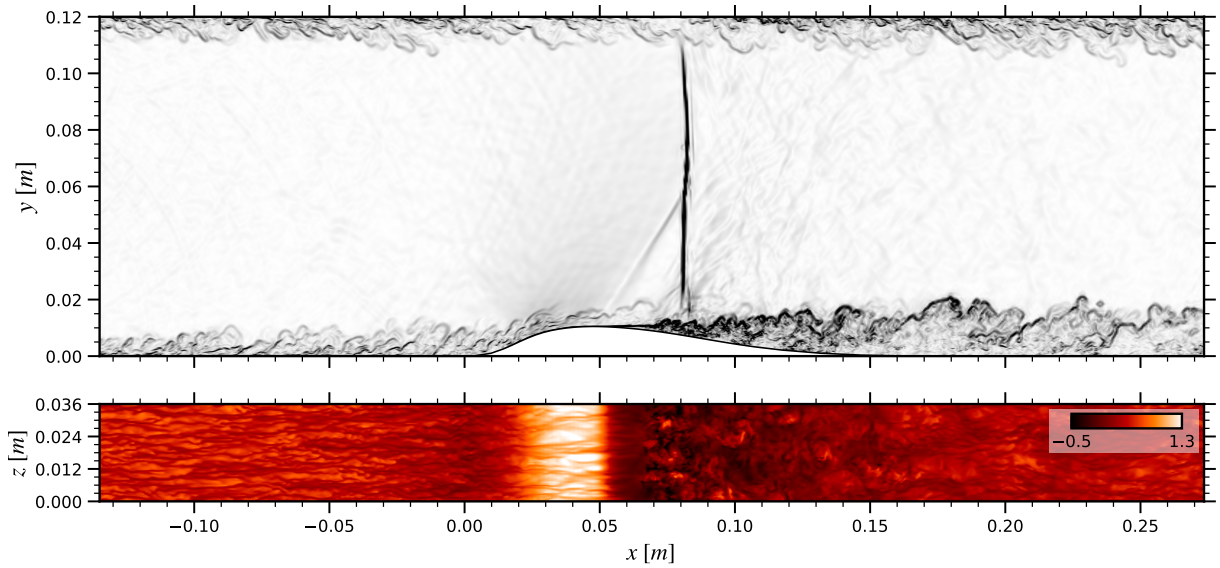


Figure 2: **Instantaneous density gradient magnitude at mid-span (*top*) and $u/U_\infty$ near the bump wall, $y^+ \approx 10$ (*bottom*).**

order flux reconstruction approach, the grid resolution is evaluated hereunder with respect to the solution points, here at polynomial order 3. In the streamwise direction, the cell size is first constant and leads to $\Delta_x^+$ = 16, in wall units based on upstream conditions. Over the last $10\delta_0$, the mesh is progressively coarsened to $\Delta_x^+$ = 160 to dampen high-frequency reflected waves. In the spanwise direction, $\Delta_z^+$ = 12. The mesh is stretched in the wall-normal direction. Bottom and top boundary layers comprise 100 solution points each, the first one located well below $y^+ = 1$. From the edge of the boundary layers and in the freestream, $\Delta_y^+$ = 16. The total number of degrees of freedom rises to approximately 80 million.

The inlet boundary is fully subsonic, with total pressure, total temperature and velocity direction imposed. These profiles, as well as Reynolds stress profiles (needed for the digital filtering approach), are taken from the averaged solution of a precursor ILES of a turbulent boundary layer in the same flow conditions. The top and bottom boundaries are no-slip adiabatic walls and periodic boundary conditions are imposed in the spanwise direction. A spatially constant static pressure is imposed along the fully subsonic outlet boundary.

Finally, the explicit time step is $4 \times 10^{-8}$s and corresponds to a CFL number of around 2.5. The parameters of the shock-capturing technique (see Goffart et al. (2022)) are $s_0$ = -4.5, $\kappa$ = 1.5, $C_T$ = 0.01 and $s_{D,0}$ = 0.2. Density is used as the sensor variable. The simulation is run over 10 periods after the transient phase. The data are collected every 50 iterations and are span-averaged to benefit from the homogeneity of the flow in that direction. This greatly helps to improve the convergence of the results.

## RESULTS

Instantaneous views of the flow field are given in figure 2. The top and bottom figures show respectively the numerical Schlieren at mid-span and the streamwise velocity near the bump wall, at $y^+ \approx 10$. Upstream of the bump, the boundary layer is fully turbulent and is characterized by thin and elongated structures. Reaching the bump, the flow first decelerates and then

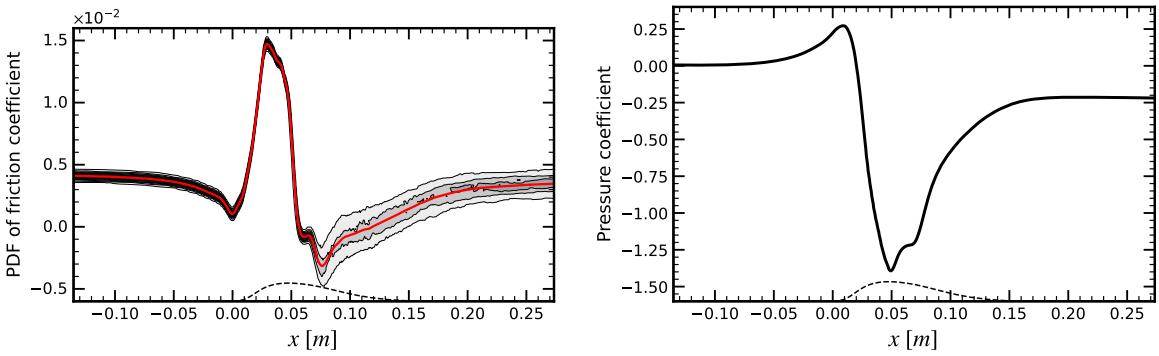


Figure 3: **Mean friction coefficient (*solid red line*) with superimposed PDF, 8 equally-spaced contours between 0.02 and 0.40 (*left*) and mean wall pressure coefficient (*right*). The *dashed line* represents the bump geometry.**

quickly accelerates over its convex part. The acceleration parameter (Jones & Launder, 1972) exceeds there the typical threshold value of $3.2\times10^{-6}$ with a peak value $\approx 2.4\times10^{-5}$. This is an indication of partial re-laminarization, which is also witnessed by wider structures. The drastic change in streamwise velocity marks the flow separation, generating an oblique compression wave that joins the normal shock at around mid-height. Further downstream, the separated shear layer becomes unstable and breaks down to turbulence, which produces additional weak compression waves that can be seen at the root of the normal shock. Past the shock, the flow is highly unsteady. Finally, approaching the end of the domain, thin and elongated structures are slowly recovered.

Figure 3 depicts the mean friction coefficient with its PDF and the mean pressure coefficient on the bump wall. It is first noticed that the extent of the upstream influence of the bump is relatively large. However, the domain is long enough upstream to let the friction coefficient steadily decrease, sign of a developed boundary layer. A long separated region can be noticed, ranging from $x \approx 0.055$m to $x \approx 0.119$m. The PDF shows actually that it consists of two parts. The first one is stable as it is associated with low variance. On very rare occasions, it almost reattaches (at $x \approx 0.065$m). The second part exhibits a much higher variance that is linked to the vortex shedding occurring at the breakdown of the shear layer. The pressure coefficient illustrates the upstream influence of the bump as well. The pressure gradually increases before sharply decreasing over the convex part of the bump. Starting from the section throat, pressure rises again, first because of the oblique compression wave and then because of the normal shock.

In the next subsections, the attention is focused on the influence of the oscillating backpressure on the flow field.

**Shock motion**

The shock position, taken as the location of maximum pressure gradient for each horizontal grid line, has been monitored during the simulation. Figure 4 displays the results from FFT, that is to say the map of shock motion amplitude and the phase at the forcing frequency, in the range of height for which the shock detection is successful. It shows that the shock behaves differently below and above $y \approx 0.075$m. The lower part of the shock exhibits only one peak at the forcing frequency whereas up to three harmonics are contributing to the motion of the

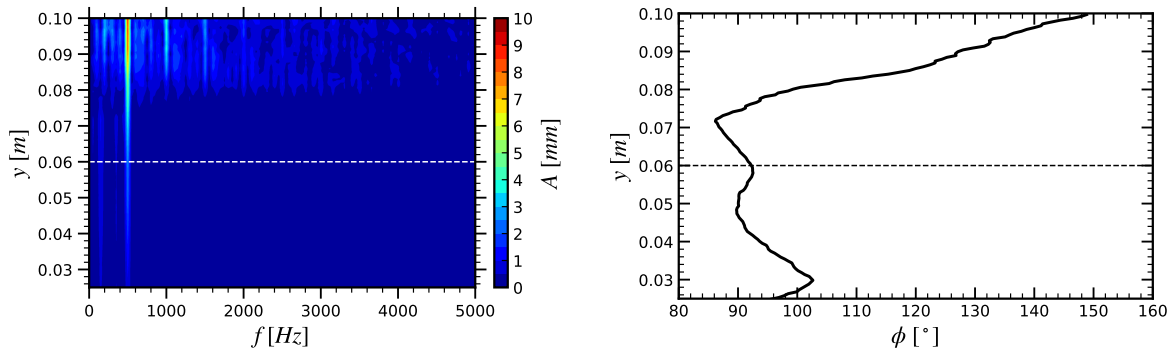


Figure 4: **Shock motion amplitude map (*left*) and phase at 500 Hz (*right*). The *dashed line* indicates the height at which the weak oblique compression wave joins the normal shock.**

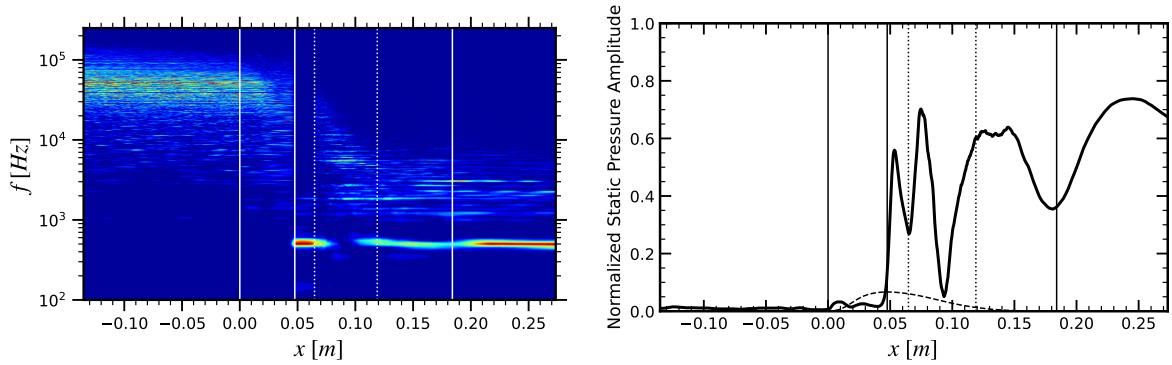


Figure 5: **Pre-multiplied WPSD map of wall pressure (*left*) and normalized wall static pressure amplitude at 500 Hz (*right*). The *vertical lines* indicate, from left to right, the beginning of the bump, the bump throat, the end of the stable separated region, the reattachment point and the end of the bump. The *dashed line* represents the bump geometry.**

upper part. At the forcing frequency, the amplitude steadily increases from around 1mm for the lowest point to 10mm for the highest one. Moreover, the phase indicates that the lower part moves in phase whereas the higher part is in advance, resulting in a wavy global motion of the shock. This different behavior is due to the oblique compression wave joining the normal shock at around mid-height and which brings additional stability through the mean flow gradients.

**Wall pressure, separation and reattachment points**

Figure 5 displays on the left the pre-multiplied WPSD map of wall static pressure. The vertical lines indicate, from left to right, the beginning of the bump, the bump throat, the end of the stable separated region, the reattachment point and the end of the bump. Upstream of the interaction, a large ridge is observed around $f \approx 50$kHz and is related to the boundary layer. Once it separates, the forcing frequency is the dominant contributor to the variance of the pressure signal. On the right of figure 5 is illustrated the wall static pressure amplitude at the forcing frequency, normalized by the amplitude of the backpressure. A complex pattern of pressure fluctuations amplification and attenuation is depicted. Nevertheless, some peaks can be linked to above-mentioned features. The first amplification peak is located at $x \approx$

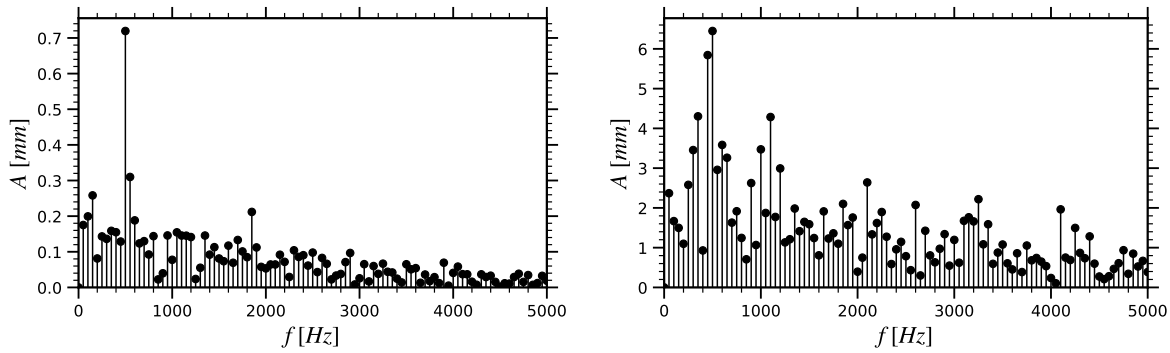


Figure 6: **Amplitude of motion of separation point (*left*) and reattachment point (*right*).**

$0.055$m, corresponding to the mean separation point, whereas the second amplification peak ($x \approx 0.075$m) can be linked to the minimum of friction coefficient. It can also be noted that the first attenuation peak ($x \approx 0.065$m) is related to the end of the stable separated region and that the third attenuation peak is located near the end of the bump, at $x \approx 0.18$m.

Figure 6 depicts the amplitude of motion of the separation and reattachment points, obtained by FFT. The main contribution comes clearly from the forcing frequency in both cases. However, many side contributions are observed for the reattachment point. The reason for this is the high variance featured in figure 3 and which is due to the vortex shedding occurring in this region. The amplitude for the reattachment point is one order of magnitude higher than for the separation point, further confirming the stable characteristic of the latter compared to the former.

**Coherent turbulent stresses**

The effect of the oscillating backpressure on the turbulent stresses is assessed in this section. The triple decomposition of Reynolds and Hussain (1972) is adopted for this analysis. Any flow quantity $q$ can be written as the sum of three components,

$$q = \overline{q} + \widetilde{q} + q' \tag{1}$$

where $\overline{q}$ is the mean component, $\widetilde{q}$ is the coherent (or harmonic) component and $q'$ is the incoherent component. Both $\widetilde{q}$ and $q'$ vary in time but the former is associated with a large time scale (a low frequency) whereas the latter corresponds to higher frequencies. This decomposition is relevant in the current work since the frequency of the fluctuating backpressure is much lower than the characteristic frequency of the turbulence in the boundary layer. Applied to the turbulent stresses, this gives

$$u_i'u_j' = \overline{u_i'u_j'} + \widetilde{u_i'u_j'} + \left(u_i'u_j'\right)' \tag{2}$$

and therefore the quantity of interest for the analysis is $\widetilde{u_i'u_j'}$, that is to say the coherent component of turbulent stresses.

From a practical point of view, the mean component of the flow is obtained by time-averaging, whereas phase-averaging will be used to extract the sum of the mean and the coherent components. The coherent motion is therefore isolated by subtracting time- and phase-averaged

flow fields. In the same way as for Reynolds stresses, a practical formulation can be derived for the coherent turbulent stresses, that is

$$\widetilde{u_i'u_j'} = \widetilde{u_i u_j} - \overline{u}_i\widetilde{u}_j - \widetilde{u}_i\overline{u}_j - \widetilde{u}_i\widetilde{u}_j + \widetilde{\widetilde{u}_i\widetilde{u}_j} \tag{3}$$

The reference oscillator for the phase-averaging is built on the location of the separation point by reconstructing the original signal using the amplitude and the phase at the forcing frequency only. This is illustrated in figure 7. Each cycle of the reconstructed signal is then divided into 10 bins of equal width and the samples of the flow field are classified and averaged accordingly. The choice of the separation point location as a reference is justified first by the fact that the major contribution is at the forcing frequency. In addition, and more importantly, the study is focused on the recirculation region directly downstream of the separation point, which is also expected to be the point of formation of coherent structures. A better description of the coherent flow will therefore be obtained as the phase difference between the reference and the region of interest is reduced. The shock position, for example, also exhibits a major contribution from the forcing frequency. However, the lowest point of the shock moves with around 60° in advance of the separation point. Using it as a criterion would have resulted in a translation of the reconstructed signal and therefore an improper classification of the samples.

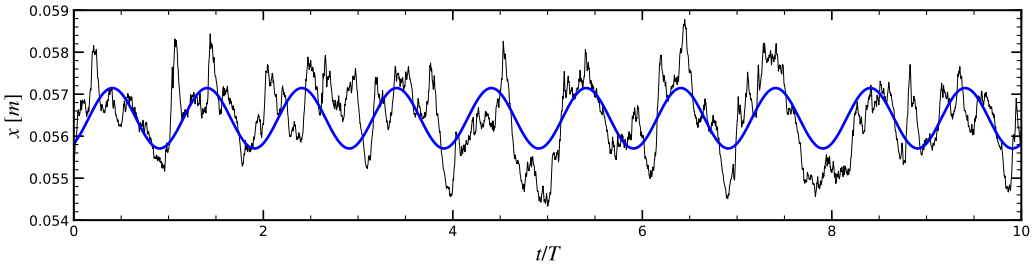


Figure 7: **Separation point location (*solid black line*) and reconstructed signal at 500 Hz (*solid blue line*).**

The results for $u'u'$ are illustrated in figure 8. Top and bottom plots show the coherent components for bin 2 (most downstream separation point) and bin 7 (most upstream separation point) respectively whereas the central plot depicts the mean component. Looking first at the top figure, different structures of coherent stress are easily noticed. Starting from the separation point, two layers are discerned. The upper layer consists of a single and elongated structure whereas the inner layer is constituted of several, smaller structures of alternating signs. The first of these is of opposite sign compared to the upper structure. The upper structure is also stronger, as it exhibits a larger magnitude. No structure is found upstream of the separation point, which indicates that it is the point of structure formation. A good convergence is obtained for structures in its vicinity whereas the identification becomes more difficult downstream and would require more samples of the flow. This is a direct consequence of the increasing dispersion in structure shape, size and strength as they are convected (Hussain, 1983). An inversion of sign is observed between the two bins, which allows to identify the same two-layers pattern in the bottom figure. It gives also a good confidence in the way the phase-averaging is performed. Finally, the coherent component is not negligible. Even though the maximum value is one order of magnitude lower than the mean component, the picture changes completely if local values are compared. At some locations, the coherent component has been found to reach up to 60%

of the local mean value. Similar results have been found for the other turbulent stresses, namely $u'v'$, $v'v'$ and $w'w'$ but are not shown for the sake of brevity.

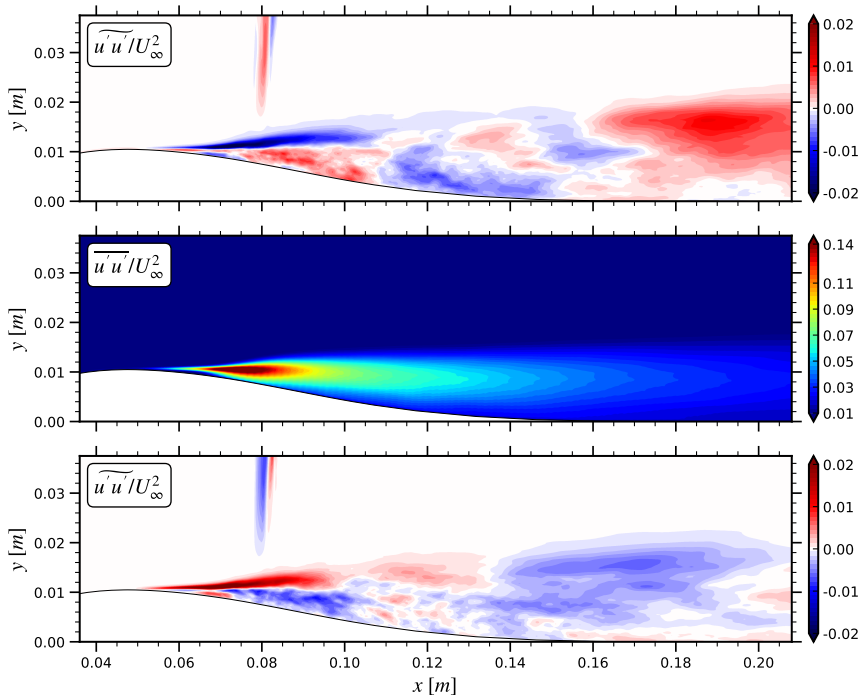


Figure 8: **Coherent component of $u'u'$ for bin 2 (*top*), mean component of $u'u'$ (*center*) and coherent component of $u'u'$ for bin 7 (*bottom*).**

## CONCLUSIONS

An investigation of the influence of the forced oscillation of the transonic flow over a bump has been performed, using results from an implicit large-eddy simulation.

The forcing frequency is found to be the main contributor in the behavior of all the flow features, from the shock motion to the separation and reattachment point locations. Complex patterns of attenuation and amplification of static pressure amplitude have also been detected at the wall.

A phase-average has been carried out considering as the reference oscillator the reconstructed signal of the separation point location at the forcing frequency. It allowed to extract the coherent component of the turbulent stresses. A two-layers pattern is observed, with a single and strong upper structure, while the inner layer shows smaller structures of alternating sign. Moreover, these components are non-negligible in comparison to the mean components.

These results highlight that special care should be given to the coherent turbulent stresses, especially regarding their modeling. This would be beneficial for frequency-domain methods, popular in turbomachinery for their reduced cost with respect to full unsteady computations. Future work is about conducting a deeper analysis of the results, in order to provide better insights for turbulence modelers.

## ACKNOWLEDGEMENTS

This project has received funding from the European Union's Horizon 2020 research and innovation programme under the grant agreement MSCA-ITN-ETN TEAMAero No 860909.

## REFERENCES

Adler, M. C., Gonzalez, D. R., Stack, C. M., & Gaitonde, D. V. (2018). Synthetic Generation of Equilibrium Boundary Layer Turbulence from Modeled Statistics. *Computers & Fluids*, *165*, 127–143. https://doi.org/10.1016/j.compfluid.2018.01.003

Bodin, O., & Fuchs, L. (2008). Shock Unsteadiness and Shock Induced Separation at Transonic Flow over a Bump. *38th Fluid Dynamics Conference and Exhibit*, 4174. https://doi.org/10.2514/6.2008-4174

Bron, O. (2003). *Numerical and Experimental Study of the Shock-Boundary Layer Interaction in Transonic Unsteady Flow* (Doctoral dissertation). Royal Institute of Technology, Sweden.

Brouwer, J. (2016). *A Study of Transonic Shock-Wave/Boundary-Layer Interactions Using Conservative, Skew-Symmetric Finite-Differences* (Doctoral dissertation). Technische Universitaet Berlin, Germany.

Carpenter, M. H., & Kennedy, C. A. (1994). *Fourth-Order 2N-storage Runge-Kutta Schemes* (Report No. NASA-TM-109112).

Ducros, F., Ferrand, V., Nicoud, F., Weber, C., Darracq, D., Gacherieu, C., & Poinsot, T. (1999). Large-Eddy Simulation of the Shock/Turbulence Interaction. *Journal of Computational Physics*, *152*(2), 517–549. https://doi.org/10.1006/jcph.1999.6238

Goffart, N., Tartinville, B., Puri, K., Hirsch, C., & Pirozzoli, S. (2022). High-Order, High-Fidelity Simulation of Unsteady Shock-Wave/Boundary Layer Interaction Using Flux Reconstruction. *8th European Congress on Computational Methods in Applied Sciences and Engineering*. https://doi.org/10.23967/eccomas.2022.138

He, L., & Ning, W. (1998). Efficient Approach for Analysis of Unsteady Viscous Flows in Turbomachines. *AIAA Journal*, *36*(11), 2005–2012. https://doi.org/10.2514/2.328

Hussain, A. F. (1983). Coherent Structures — Reality and Myth. *The Physics of Fluids*, *26*(10), 2816–2850. https://doi.org/10.1063/1.864048

Huynh, H. T. (2007). A Flux Reconstruction Approach to High-Order Schemes Including Discontinuous Galerkin Methods. *18th AIAA Computational Fluid Dynamics Conference*, 4079. https://doi.org/10.2514/6.2007-4079

Jones, W. P., & Launder, B. E. (1972). The Prediction of Laminarization with a Two-Equation Model of Turbulence. *International Journal of Heat and Mass Transfer*, *15*(2), 301–314. https://doi.org/10.1016/0017-9310(72)90076-2

Klein, M., Sadiki, A., & Janicka, J. (2003). A Digital Filter Based Generation of Inflow Data for Spatially Developing Direct Numerical or Large Eddy Simulations. *Journal of Computational Physics*, *186*(2), 652–665. https://doi.org/10.1016/S0021-9991(03)00090-1

Lund, T. S., Wu, X., & Squires, K. D. (1998). Generation of Turbulent Inflow Data for Spatially-Developing Boundary Layer Simulations. *Journal of Computational Physics*, *140*(2), 233–258. https://doi.org/10.1006/jcph.1998.5882

Persson, P.-O., & Peraire, J. (2006). Sub-Cell Shock Capturing for Discontinuous Galerkin Methods. *44th AIAA Aerospace Sciences Meeting and Exhibit*, 112. https://doi.org/10.2514/6.2007-4079

Reynolds, W., & Hussain, A. (1972). The Mechanics of an Organized Wave in Turbulent Shear Flow. Part 3. Theoretical Models and Comparisons with Experiments. *Journal of Fluid Mechanics*, *54*(2), 263–288. https://doi.org/10.1017/S0022112072000679

Sigfrids, T. (2003). *Hot Wire and PIV Studies of Transonic Turbulent Wall-Bounded Flows* (Licentiate Thesis). Royal Institute of Technology, Sweden.

Tucker, P. (2011). Computation of Unsteady Turbomachinery Flows: Part 1—Progress and Challenges. *Progress in Aerospace Sciences*, *47*(7), 522–545. https://doi.org/10.1016/j.paerosci.2011.06.004

Wang, C., Zhang, X., Shu, C. W., & Ning, J. (2012). Robust High Order Discontinuous Galerkin Schemes for Two-Dimensional Gaseous Detonations. *Journal of Computational Physics*, *231*(2), 653–665. https://doi.org/10.1016/j.jcp.2011.10.002

Wollblad, C., Davidson, L., & Eriksson, L.-E. (2006). Large Eddy Simulation of Transonic Flow with Shock Wave/Turbulent Boundary Layer Interaction. *AIAA Journal*, *44*(10), 2340–2353. https://doi.org/10.2514/1.20358

Wollblad, C., Davidson, L., & Eriksson, L.-E. (2010). Investigation of Large Scale Shock Movement in Transonic Flow. *International Journal of Heat and Fluid Flow*, *31*(4), 528–535. https://doi.org/10.1016/j.ijheatfluidflow.2010.02.009

Xie, Z. T., & Castro, I. P. (2008). Efficient Generation of Inflow Conditions for Large Eddy Simulation of Street-Scale Flows. *Flow, Turbulence and Combustion*, *81*(3), 449–470. https://doi.org/10.1007/s10494-008-9151-5